















K-CONTACT DISTANCE FOR NOISY NONHOMOGENEOUS SPATIAL POINT DATA WITH APPLICATION TO REPEATING FAST RADIO BURST SOURCES

BY A. M. COOK^{1,2,a} , DAYI LI^{3,d} , GWENDOLYN M. EADIE^{1,3,4,e} , DAVID C. STENNING^{5,g} , PAUL SCHOLZ^{6,2,i} , DEREK BINGHAM^{5,h}, RADU CRAIU^{3,f} , B. M. GAENSLER^{7,2,1,j} , KIYOSHI W. MASUI^{8,9,l} , ZIGGY PLEUNIS^{10,11,m} , ANTONIO HERRERA-MARTIN^{1,3,b} , RONNIY C. JOSEPH^{12,13,n} , AYUSH PANDHI^{1,2,c} , AARON B. PEARLMAN^{12,13,o} , AND J. XAVIER PROCHASKA^{7,k} 

¹David A. Dunlap Department of Astronomy & Astrophysics, University of Toronto, 50 St. George Street, Toronto, Ontario, Canada M5S 3H4, ^acook@astro.utoronto.ca; ^bantonio.herreramartin@utoronto.ca; ^cayush.pandhi@mail.utoronto.ca

²Dunlap Institute for Astronomy and Astrophysics, 50 St. George Street, University of Toronto, ON M5S 3H4, Canada

³Department of Statistical Science, University of Toronto, Ontario Power Building, 700 University Avenue, 9th Floor, Toronto, ON M5G 1Z5, ^ddayi.li@mail.utoronto.ca; ^egwen.eadie@utoronto.ca; ^fradu.craiu@utoronto.ca

⁴Data Science Institute, University of Toronto, 700 University Ave 10th floor, Toronto, ON M5G 1Z5

⁵Department of Statistics and Actuarial Science, Simon Fraser University, 8888 University Dr W, Burnaby, BC V5A 1S6, Canada, ^gdavid_stenning@sfu.ca; ^hdbingham@sfu.ca

⁶Department of Physics and Astronomy, York University, 4700 Keele Street, Toronto, Ontario, M3J 1P3, Canada, ⁱpscholz@yorku.ca

⁷Department of Astronomy and Astrophysics, University of California, Santa Cruz, 1156 High Street, Santa Cruz, CA 95064, ^jgaensler@ucsc.edu; ^kxavier@ucolick.org

⁸MIT Kavli Institute for Astrophysics and Space Research, Massachusetts Institute of Technology, 77 Massachusetts Ave, Cambridge, MA 02139, USA, ^lkmasui@mit.edu

⁹Department of Physics, Massachusetts Institute of Technology, 77 Massachusetts Ave, Cambridge, MA 02139, USA

¹⁰Anton Pannekoek Institute for Astronomy, University of Amsterdam, Science Park 904, 1098 XH Amsterdam, The Netherlands, ^mz.pleunis@uva.nl

¹¹ASTRON, Netherlands Institute for Radio Astronomy, Oude Hoogeveensedijk 4, 7991 PD Dwingeloo, The Netherlands

¹²Department of Physics, McGill University, 3600 rue University, Montréal, QC H3A 2T8, Canada, ⁿronniy.joseph@mcgill.ca; ^oaaron.b.pearlman@physics.mcgill.ca

¹³Trottier Space Institute, McGill University, 3550 rue University, Montréal, QC H3A 2A7, Canada

This paper introduces an approach to analyze nonhomogeneous Poisson processes (NHPP) observed with noise, focusing on previously unstudied second-order characteristics of the noisy process. Utilizing a hierarchical Bayesian model with noisy data, we estimate hyperparameters governing a physically motivated NHPP intensity. Simulation studies demonstrate the reliability of this methodology in accurately estimating hyperparameters. Leveraging the posterior distribution, we then infer the probability of detecting a certain number of events within a given radius, the k -contact distance. We demonstrate our methodology with an application to observations of fast radio bursts (FRBs) detected by the Canadian Hydrogen Intensity Mapping Experiment’s FRB Project (CHIME/FRB). This approach allows us to identify repeating FRB sources by bounding or directly simulating the probability of observing k physically independent sources within some radius in the

Keywords and phrases: Astrostatistics (1882), Interdisciplinary astronomy (804), Poisson distribution (1898), Spatial point processes (1915), Astrostatistics techniques (1886).

detection domain, or the *probability of coincidence* (P_C). The new methodology improves the repeater detection P_C in 86% of cases when applied to the largest sample of previously classified observations, with a median improvement factor (existing metric over P_C from our methodology) of ~ 3000 .

1. Introduction.

1.1. *Nonhomogeneous Poisson Point Processes.* To learn about the nature of unknown astrophysical phenomena, astrophysicists can search for connections between different sources or across populations. A question of interest to astrophysicists is often: How do we estimate the likelihood of two or more spatially coincident, but separated in time, events being physically related when measurement uncertainty on event positions is non-negligible, the probability of detection varies on the sky, and the data is noisy? These connections, in particular spatial coincidences, can be ambiguous owing to instrumentation limitations, observational biases, and the sheer number of objects in the Universe. Such complicating factors often lead to non-homogeneous spatial point processes that are observed with noise.

Considerable effort has gone into modelling noisy nonhomogeneous Poisson processes (NHPPs; [Van Lieshout, 2000](#)), particularly in ecology. For example, [Cucala \(2008\)](#) presented an edge-corrected deconvoluting kernel estimator for the intensity of noisy and nonhomogeneous spatial data and a bandwidth selection procedure for that kernel estimator. [Chakraborty and Gelfand \(2010\)](#) also estimated the two dimensional intensity of an NHPP observed with Gaussian noise. In their work, the authors derived the likelihood function for the intensity of an NHPP observed with noise, also considering the effect of events which, due to the stochastic error, are moved inside or outside of the observed domain and hence cause miss-estimation of the intensity near these boundaries. While these approaches allow for descriptions of an NHPP intensity function from noisy data, neither methods are used to make predictive inferences about second order characteristics.

On the other hand, [Lund, Penttinen and Rudemo \(1999\)](#) and [Bar-Hen et al. \(2013\)](#) made inferences based on observations from noisy NHPPs with numerically estimated second order characteristics, (e.g., the nearest-neighbor function). In those works, however, the authors were interested in recovering these second order characteristics for the underlying unobserved homogeneous Poisson process from the noisy observations, and not those of the observed noisy process itself. For astrophysicists that are interested in quantifying the probability of observing spatially coincident and separate in time, but ultimately physically unrelated noisy events, the unobserved NHPP is not the process of interest.

In this paper, we propose a hierarchical Bayesian model for noisy observations to estimate an NHPP intensity function with the purpose of making predictive inference on the *noisy process*. Existing statistical methodologies seek only to make inferences on the underlying or true process given noisy observations of it. We first construct a hierarchical Bayesian model of a parameterized Poisson intensity function that is motivated by the data-collecting instrument (in our application, a telescope). We then use this intensity function to estimate the probability of observing two or more ($k \geq 2, k \in \mathbb{N}$) events within a given observed radius in the noisy NHPP assuming they are physically independent: the k -contact distance. This probability is estimated both using direct simulation and a novel and analytic probability bound we derive on the k -contact distance for the noisy NHPP. This then allows us to estimate the probability that the k physically independent events are within some radius (in the observation domain) of one another and, if sufficiently improbable, give evidence that two or more events may more plausibly be caused by the same source, meaning the same astrophysical body or system, as opposed to sources that sit nearby each other in the observation

domain. While this methodology is geared towards astrophysical observations with significant localization uncertainty, the common application of NHPPs to fields like ecology and epidemiology suggests that the method may be beneficial for research in other disciplines, for example, hotspot detection.

1.2. Motivating Application. Fast radio bursts (FRBs) are short, bright, extragalactic radio signals of unknown origin. Our motivation for the proposed methodology is to distinguish clusters of physically unrelated but spatially coincident FRB sources from true *repeating* FRB sources, which we describe next.

Many source models have been proposed for FRBs, often drawing connections to exotic populations like neutron stars and black holes (e.g., [Platts et al., 2019](#); [Petroff, Hessels and Lorimer, 2022](#); [Zhang, 2022](#)). While the majority of FRBs have been observed to happen once, a minority are observed to repeat. That is, multiple bursts (signals) from one location in the sky are observed, presumably from the same source (e.g. [Spitler et al., 2016](#); [CHIME/FRB Collaboration, 2019a,b, 2023](#); [Fonseca et al., 2020](#); [Niu et al., 2022](#)). The discovery of repeating sources, or *repeaters*, suggests that at least some of the extremely luminous bursts need to be sourced from non-cataclysmic events where the source is not consumed as a result of the production of the burst. There are still many proposed theories for this repetition, but the non-cataclysmic nature of the events significantly narrows the number of possible source models for these repeaters.

Astronomers have detected and published 790 distinct sources of FRBs on the sky, of which 56 are known repeaters¹. The most prolific repeaters have been observed to repeat hundreds to thousands of times, while dozens have just two or three total observed bursts (e.g. [Li et al., 2021](#); [CHIME/FRB Collaboration, 2023](#)). While there is some evidence that repeating FRBs are a distinct population from apparent non-repeating FRBs ([Pleunis et al., 2021](#)), it is not known definitively whether there are two separate populations or if all FRBs repeat ([James, 2023](#); [Kirsten et al., 2024](#)).

Most FRB sources detected to date, repeating or otherwise, have been discovered by the Canadian Hydrogen Intensity Mapping Experiment (CHIME). A traditional telescope will point to a small patch of the sky and track that position over time. CHIME is a transit radio telescope, meaning it has no moving parts and simply observes the sky passing overhead ([CHIME Collaboration, 2022](#)). The CHIME telescope collects radio signal data (voltages) this way and then uses digital signal processing to mimic multiple traditional telescopes by generating ‘beams’ on the sky to search for FRB signals ([CHIME/FRB Collaboration, 2018](#)).

The stationary design of CHIME has observational benefits, like a large field-of-view and daily monitoring of sources, as well as challenges, such as exposure that is uneven on the sky. At the same time, CHIME has limited angular resolution, that is, ability to pinpoint exactly where the sources are located on the sky. The FRB project of CHIME (CHIME/FRB) observes FRBs with 99.7% localization (sky position) uncertainty regions that span, at best, a few tens of square arcminutes², or at worst a few square degrees. FRBs are found within galaxies, and it is physically reasonable that multiple independent FRB sources could be found in a localization region of this size since there are typically many galaxies (which could host FRBs) within these regions³.

¹<https://www.wis-tns.org/> accessed Sept 25th, 2024

²For a sense of scale, the full Moon subtends ~ 30 arcminutes, and one arcminute is, by definition, $1/60$ degrees.

³The well-known Hubble Ultra Deep Field image, in which every non-spiky point of light is a galaxy ($\sim 10,000$ such galaxies), is of comparable size to CHIME/FRB’s smallest (best constrained) localization regions ([Beckwith et al., 2006](#)).

Symbol	Description
\mathbf{Y}	point process of observed (noisy) positions
$\mathbf{y}_1, \dots, \mathbf{y}_n$	Realization of observed positions, from random process \mathbf{Y}
$\boldsymbol{\varepsilon}_i$	spatial perturbation vector due to measurement error
n	Number of observed events
\mathbf{X}	Nonhomogeneous poisson process (true positions)
$\mathbf{x}_1, \dots, \mathbf{x}_n$	Realization of true positions, from random process \mathbf{X}
Λ	Intensity function of NHPP \mathbf{X}
$\boldsymbol{\theta}$	Hyperparameter vector governing Λ
D	Domain on which positions are defined
k	Number of events in cluster
r	Radius of the minimal bounding sphere the cluster of events
s_0	Center of minimal bounding sphere cluster of events

TABLE 1

Definitions of application-independent variables used throughout this text.

In summary, a CHIME/FRB detection does not provide the precise position of a source, and as CHIME/FRB continues to detect more FRBs, the probability that two or more spatially independent FRB sources have observed concordant positions becomes non-negligible. Ongoing upgrades to the experiment will increase the localization precision for FRBs detected by CHIME/FRB (Lanman et al., 2024). This increased localization precision usually allows for probabilistic selection between potential host galaxies, using, e.g., the ‘*Probabilistic Association of Transients to their Hosts*’ routine (PATH; Aggarwal et al., 2021), if not direct unique identification. However, there are other poorly-localized transient events whose potential association with FRBs would inform source models, such as gravitational wave sources and gamma-ray bursts (e.g., Moroiianu et al., 2023; Curtin et al., 2024).

Application of the methodology that we propose will allow observers to make a probabilistic statement about the certainty of physical association between clusters of k bursts observed with noise, i.e. potential repeaters, distinguishing them from independent sources that share overlapping localization regions on the sky. If CHIME/FRB surveyed all points in the Universe equally, making the probability of detecting FRBs spatially uniform, this process could be modeled as a three dimensional, homogeneous Poisson point process. Instead, there is uneven exposure and sensitivity in the intensity of FRB detections which is a non-trivial combination of spherical geometry, the luminosity distribution of FRBs, and instrumental effects.

The net effect is an NHPP FRB detection intensity that cannot be derived from first principles and must instead be empirically estimated from noisy telescope detections. NHPP processes are not only applicable to data from CHIME/FRB; NHPPs were first applied to FRB detections by Lawrence et al. (2017), who used an NHPP to model the rate of FRBs.

The rest of this article is organized as follows: in Section 2, we specify a hierarchical model for observed noisy event locations from an NHPP. In Section 3, we outline the inference on the probability of observing k events within a given volume in the observation domain. In Section 4, we apply this model to data from CHIME/FRB, and derive a parametrization for CHIME/FRB’s intensity function on the sky. In Section 5, we describe the implementation and the performance of a method based on Markov chain Monte Carlo (MCMC) sampling for estimating the hyperparameters’ posterior distribution. In Section 6, we implement the proposed methodology on our application. We also estimate, via direct simulation and an analytic upper bound, the probability of coincidence (P_C) for each of CHIME/FRB’s currently published repeaters and compare the probabilities to the existing measure of cluster significance used by CHIME/FRB Collaboration (2023).

2. Hierarchical Model for NHPP Observed with Noise. Let $\mathbf{X} \subseteq D \subseteq \mathbb{R}^d$ be a nonhomogeneous Poisson point process (we are concerned specifically with $d = 3$ for our application given the event positions are observed in three dimensions, but remain general for now) with intensity function $\Lambda(\mathbf{s}; \boldsymbol{\theta}) : D \rightarrow [0, \infty)$, that is,

$$(1) \quad \mathbf{X} \sim \text{NHPP}(\Lambda(\mathbf{s}; \boldsymbol{\theta})),$$

where Λ is parameterized by vector $\boldsymbol{\theta}$, and $\Lambda(\mathbf{s}; \boldsymbol{\theta})$ is defined for any event location \mathbf{s} in the bounded domain D of \mathbf{X} . By the definition of a Poisson process and its intensity function, we must have that (i) $\Lambda(\mathbf{s}; \boldsymbol{\theta})$ is a Borel measure, (ii) given any bounded Borel set $B \subseteq D$ the probability mass function for number of observed events in B , $N(B)$, is Poisson distributed with mean $\Lambda(B; \boldsymbol{\theta})$, and (iii) for any j disjoint bounded Borel sets B_1, \dots, B_j , the random variables $N(B_1), \dots, N(B_j)$ are independent (Van Lieshout, 2000).

Following Chakraborty and Gelfand (2010), but under the simplifying assumption that events can not jump into or out of the domain due to stochastic error in our model, we also assume that no two events can share the same position, i.e., \mathbf{X} is a *simple* point process or Λ is atomless. This is a null assumption in our application. Given these properties, conditional on the number of events n in D , the locations $\mathbf{x}_1, \dots, \mathbf{x}_n$ are independent draws from $\lambda(\mathbf{s}|\boldsymbol{\theta}) = \frac{1}{C} \Lambda(\mathbf{s}; \boldsymbol{\theta})$, where $C \in \mathbb{R}$ is the constant which normalizes $\Lambda(\mathbf{x}_i; \boldsymbol{\theta})$ to a density over D (Kottas and Sansó, 2007; Chakraborty and Gelfand, 2010). That is, the joint distribution of n and $\mathbf{X} = \{\mathbf{x}_1, \dots, \mathbf{x}_n\}$, conditional on $\boldsymbol{\theta}$ is:

$$(2) \quad L(\boldsymbol{\theta}|n; \mathbf{x}_1, \dots, \mathbf{x}_n) \propto e^{-\int_D \Lambda(\mathbf{s}; \boldsymbol{\theta}) d\mathbf{s}} \frac{\prod_{i=1}^n \Lambda(\mathbf{x}_i; \boldsymbol{\theta})}{n!}.$$

The above follows from the conditional likelihood of $\mathbf{x}_1, \dots, \mathbf{x}_n \propto \prod_i \lambda(\mathbf{x}_i|\boldsymbol{\theta})$ and probability mass function for the number of observed events, n , being

$$(3) \quad f(n|\Lambda, \boldsymbol{\theta}) = \frac{\left(\int_D \Lambda(\mathbf{s}; \boldsymbol{\theta}) d\mathbf{s}\right)^n}{n!} \exp\left(-\int_D \Lambda(\mathbf{s}; \boldsymbol{\theta}) d\mathbf{s}\right).$$

We derive the specific form of Λ for the CHIME/FRB experiment in Section 4, but this is left general at this stage.

Let $\mathbf{Y} = \{\mathbf{y}_1, \dots, \mathbf{y}_n\}$ be a point process of n noisy event locations, which are a perturbed set of the n true event locations from \mathbf{X} :

$$(4) \quad \mathbf{y}_i = \mathbf{x}_i + \boldsymbol{\varepsilon}_i,$$

where $\boldsymbol{\varepsilon}_i$ is a random vector in \mathbb{R}^3 that describes the spatial perturbation due to measurement error. We do not assume this is Gaussian, as in previous works, but instead leave the error distribution general. The distribution of $\boldsymbol{\varepsilon}_i$ for our application is empirically estimated, and the details are deferred to Section 4.4.

Our hierarchical model can thus be summarized as follows:

$$\begin{aligned} \text{Stage I} \quad & \mathbf{y}_i | \mathbf{x}_i, \boldsymbol{\varepsilon}_i \stackrel{\text{ind}}{\sim} f(\cdot) \\ \text{Stage II} \quad & \mathbf{x}_i | n \stackrel{\text{ind}}{\sim} \lambda(\mathbf{s}, \boldsymbol{\theta}) \\ \text{Stage III} \quad & n | \Lambda \sim \text{Pois} \left(\int_D \Lambda(\mathbf{s}, \boldsymbol{\theta}) d\mathbf{s} \right). \end{aligned}$$

A summary of the notation we use is given in Table 1. We can thus write the full likelihood function of the above model as:

$$(5) \quad L(n; \mathbf{x}_1, \dots, \mathbf{x}_n | \boldsymbol{\theta}) = \frac{1}{n!} \exp\left(-\int_D \Lambda(\mathbf{s}, \boldsymbol{\theta}) d\mathbf{s}\right) \left[\prod_{i=1}^n \Lambda(\mathbf{x}_i, \boldsymbol{\theta}) \right] \left[\prod_{i=1}^n f(\mathbf{y}_i | \mathbf{x}_i) \right],$$

where $f(\mathbf{y}_i | \mathbf{x}_i)$ is the p.d.f. in Stage I evaluated at \mathbf{y}_i .

3. Bounding the Probability of Coincidence for Noisy NHPPs. We want to quantify the likelihood of observing k noisy event locations close together in our observation domain assuming the model outlined in Section 2: that the events are conditionally independent, or in our application, physically unrelated, in order to identify unlikely clusters.

We can use the posterior distribution of the model parameters to estimate the probability of observing k conditionally independent events in some closed hypersphere $b(s_0, r)$ with center s_0 and radius r . For \mathbf{X}, \mathbf{Y} defined as in Section 2, we want to compute

$$(6) \quad P(d_k(s_0, \mathbf{Y}) \leq r)$$

where $d_k(s_0, \mathbf{Y})$ denotes the distance from s_0 to the k^{th} nearest point in \mathbf{Y} . The observed NHPP \mathbf{Y} can only be expressed through the true NHPP \mathbf{X} , and ultimately the probability of observing k events within some observed radius will depend on the density of the bounding radius of the unobserved true event positions. Thus the probability in Equation 6 cannot be computed directly given the uncertainties in the true positions of the events (otherwise, without noise, this probability could be computed directly using Equation 9, reproduced from [Berman 1977](#)). Instead, we bound the probability from above using the first result of Proposition 1, derived in Appendix A:

$$(7) \quad P(d_k(s_0, \mathbf{Y}) \leq r) \leq \int_{\varepsilon_1} \cdots \int_{\varepsilon_k} \left\{ 1 - \sum_{i=0}^{k-1} \frac{\left(\int_{B(s_0, \tilde{r})} \Lambda(s) \mu(ds) \right)^i}{i!} \times \right. \\ \left. \exp \left(- \int_{B(s_0, \tilde{r})} \Lambda(s) \mu(ds) \right) \right\} f(\{\varepsilon_i\}_{i=1}^k) \mu(d\varepsilon_1) \cdots \mu(d\varepsilon_k)$$

where $\tilde{r} = r + \max\{|\varepsilon_i| : 1 \leq i \leq k\}$, $f(\{\varepsilon_i\}_{i=1}^k)$ is the joint p.d.f. of $\{\varepsilon_i\}_{i=1}^k$. Written as the bound of an integral, ε_i implies the support of ε_i , and μ is the Lebesgue measure.

This bound assumes the most conservative case for a given observed radius r and k drawn error displacements: that the largest of those k errors reduced the true (unobserved) k -contact radius by the magnitude of the largest error displacement. This maximally increases the probability of k events happening in the true NHPP, hence the bound.

Of course, for all but the most well-behaved $f(\{\varepsilon_i\}_{i=1}^k)$ this integral would need to be computed numerically by sampling from $f(\{\varepsilon_i\}_{i=1}^k)$. If one can sample from the error distribution, one can sample from the joint distribution of true positions, and hence directly simulate the left hand side of Equation 7. However, the bound in Equation 7 has the additional property that, when the ε_i are i.i.d., it can be further simplified to

$$P(d_k(s_0, \mathbf{Y}) \leq r) \leq \int_0^\infty \left\{ 1 - \sum_{i=0}^{k-1} \frac{\left(\int_{B(s_0, r+x)} \Lambda(s) \mu(ds) \right)^i}{i!} \times \right. \\ \left. \exp \left(- \int_{B(s_0, r+x)} \Lambda(s) \mu(ds) \right) \right\} k f_d^{k-1}(x) dx,$$

where $k f_{|\varepsilon_i|}^{k-1}(x)$ is the p.d.f. of $\max\{|\varepsilon_i| : 1 \leq i \leq k\}$ (also derived in Appendix A). This reduces the computational load by decreasing the number of d -dimensional integrations from $k+1$ to two, linearly decreasing the computation time. This would be a large effect when inferences are being made on high- k k -contact distances. In our application the ε_i are not i.i.d. and our k are small, but in Section 6.2 we compute both the bound as well as simulate directly and compare the results. In the following subsection, we explore the utility of the bound in more general applications.

3.1. *Probability bound simulations.* To determine how close the newly derived upper bound on k -contact probability is to the true k -contact distance probability, and hence the utility of the bound, we study two general intensity functions via simulations. Drawing from the first two NHPP intensity models specified by [Chakraborty and Gelfand \(2010\)](#), bivariate Gaussian and Gaussian mixture models, we simulate 50,000 datasets of 2D positions and then perturb all positions from a bivariate normal distribution, $\mathcal{N}(0, \sigma_{\text{err}}^2)$. The bivariate Gaussian density is scaled to be an NHPP intensity which integrates to 200 on its domain, and with mean vector and covariance matrix

$$\mathcal{N}\left(\begin{pmatrix} 0.64 & 0.016 & 0.007 \\ 0.61 & 0.007 & 0.02 \end{pmatrix}\right)$$

respectively. The Gaussian mixture density is also scaled to be a NHPP intensity which integrates to 200 on its domain, with two components, each a bivariate Gaussian with mean vectors and covariance matrices

$$q\mathcal{N}\left(\begin{pmatrix} 0.64 & 0.016 & 0.007 \\ 0.61 & 0.007 & 0.02 \end{pmatrix}\right) + (1-q)\mathcal{N}\left(\begin{pmatrix} 0.25 & 0.007 & 0.0005 \\ 0.14 & 0.0005 & 0.002 \end{pmatrix}\right)$$

for the first (mixing weight of $q = 0.71$) and second components respectively.

For 500 test center points (s_0) from these intensities, we then check the frequency in 50,000 simulations that 2 or more events are found within some radius, $r = 10^{-2}$, of the s_0 , setting $\sigma_{\text{err}} = 10^{-3}$. These values were chosen to explore a range of frequencies from 1.0 to a few/50,000, where 50,000 was chosen to keep simulation time tractable. We then compute the k -contact ($k = 2$ in this case) probability bound for a radius r for each s_0 .

The simulation frequency vs. probability bound can be found in the leftmost panels of [Figure 1](#), with points shaded according to the intensity value at s_0 . The probability bounds range from 0 – 13 times larger than the frequencies derived from simulations for both intensity functions in this error and radius regime. We then repeat these simulations for $\sigma_{\text{err}} = 10^{-2}$, and 10^{-1} , such that we can explore the bound in different error regimes: when error displacements are an order of magnitude smaller than the radius of interest (left-most panels), of comparable size to the radius of interest (center panels), and an order of magnitude larger than the radius of interest (right panels). We find the probability bound is closer to the true value when the test point is at lower intensity regions and when error regimes are small compared to the radii of interest.

We conclude from this simulation study that the probability bound is most similar to the true probability for radii similar to or larger than the scale of typical error displacements. If the errors considered are much larger than the k -contact distance one wishes to infer, intuitively, the bound is more likely to fail to produce interesting constraints, especially when applied in high intensity regions of the domain. In [Section 6.2](#), we perform an analysis with the same intention of quantifying the usefulness of the bound for our specific application by comparing the P_C metric from the existing methodology to that from our proposed methodology for the most recent repeater sample from [CHIME/FRB Collaboration \(2023\)](#). We show the bound is sufficiently constraining to rule out the hypothesis of k independent sources for more repeater candidates than the existing methodology.

4. Application to CHIME/FRB. In our application, the NHPP is a non-uniform intensity of FRB detection probability by CHIME/FRB. The observed FRB detection distribution is a function of the volume density of FRB sources and of the probability of actually detecting an FRB. We first introduce the coordinate system, and then introduce the necessary astrophysical quantities and concepts in order to describe the main factors that affect these distributions and to elucidate how we parameterize the intensity, Λ . The application-dependent notation is summarized in [Table 2](#).

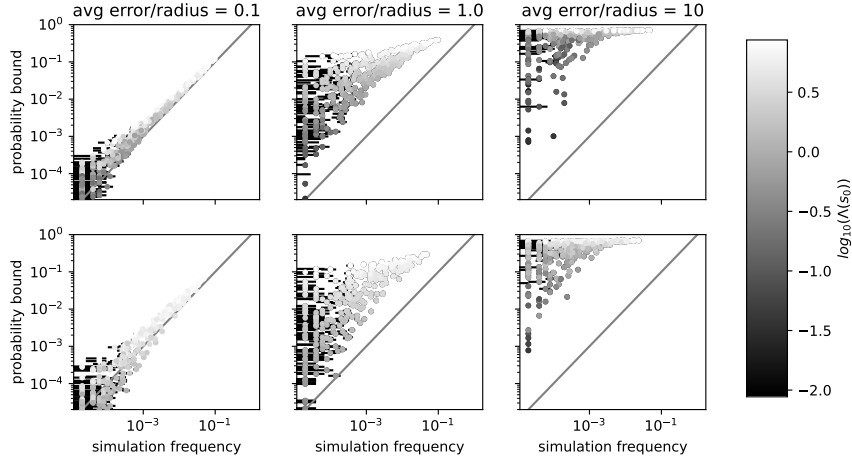


FIG 1. k -contact probability bound versus frequency from simulations of two different NHPP intensity models and in different noise regimes. In each panel, 500 test points are drawn uniformly from the domain of the experiment, and then 50,000 simulated datasets are drawn from the relevant NHPP Λ and positions are perturbed by Gaussian noise centered at $(0, 0)$ and with standard deviation of 10^{-3} , 10^{-2} , 10^{-1} for the left, center, and right columns respectively. We record the frequency of having $k = 2$ events within some radius $r = 10^{-2}$ for each simulation. We then, given s_0 , the noise distribution, and r , compute the probability bound in Equation 7. Top row: 50,000 simulations for test centers (s_0) drawn from bivariate Gaussian intensity (full parameter details can be found in Section 3.1). Bottom row: As for the top row, but simulated datasets are drawn from a bivariate Gaussian mixture intensity. A black line is drawn in each panel to denote where the bound and simulation frequency would be equal. Points are colored according to the value of the intensity at the test center, $\Lambda(s_0)$. We conclude from these simulations that the bound is most similar to the true probability bound when average noise displacements are smaller than, or of comparable size to, the k -contact distance radius of interest, and hence are more likely to provide meaningful constraints in these regimes.

Symbol	Description
ϕ	Geographical latitude of the telescope
δ	Declination, equivalent to latitude on the celestial sphere
α	Right ascension, equivalent to longitude on the celestial sphere
DM	Dispersion measure, a rough proxy for FRB distance
ζ	Zenith angle
N_{FRBs}	Poisson rate, or the integral of the intensity function Λ over the entire domain

TABLE 2

Definition of application-dependent variables used throughout this text.

4.1. *Coordinate system.* FRB positions are defined by right ascension (α), declination (δ), and dispersion measure (DM). The angles α and δ are equivalent to longitude and latitude on the celestial sphere, illustrated in Figure 2.

DM is a quantification of the significant frequency dependent delay of radio waves due to the ionized gas the waves traverse. As a line-integrated column density, DM is a proxy for distance: if two hypothetical signals from the identical point on the sky were measured to have different DMs, one would necessarily be more distant than the other because the signal with higher DM must have traversed more ionized gas. The common unit for DM of parsecs per cubic centimeter (pc cm^{-3}) is used as it is convenient for astrophysicists to determine a rough distance to a Galactic radio source given a known average Galactic electron density (in cm^{-3}), and has been subsequently adopted for extragalactic radio sources including FRBs. This is partially because the Galactic contribution to the DM of FRBs is considered a foreground contaminant and must be subtracted off in order to make meaningful conclusions

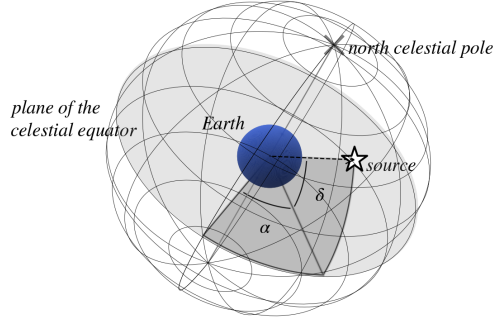


FIG 2. Illustration of right ascension (α) and declination (δ). These two angles are equivalent to longitude and latitude on the celestial sphere, respectively. α is referenced from the ‘vernal equinox’, which is one of the intersecting points of the celestial equator and the geographical equator, and α is defined here between 0 and 360 degrees. δ differs from the typical spherical coordinate polar angle as it is referenced to the $x - y$ plane, or the plane of the celestial equator, rather than the $+z$ -axis (north celestial pole). δ is defined between -90 (south celestial pole) and 90 degrees (north celestial pole).

about the distance to an FRB using DM. The Galactic contribution comes from ionized gas within the disk-shaped region of our Galaxy (where most stars are located) and the halo of our Galaxy (a much larger gas cloud surrounding this stellar disk). We subtract estimates of these contributions using a model of the density in the disk from Cordes and Lazio (2002) and estimates from Dolag et al. (2015) of the electron density halo from cosmological simulations which are supported by recent observational results (Cook et al., 2023; Ravi et al., 2023). Henceforth, it is assumed that we are referring to the Galactic-foreground subtracted value when we discuss the DMs of FRBs.

4.2. *Number of sources vs DM and δ .* Assuming a Euclidean geometry for the Universe⁴, and assuming an FRB population that has not changed as the Universe evolved over billions of years, the source volume number density should be constant as a function of distance from Earth and hence the number of sources, N_{sources} , is found by integrating the volume observed by CHIME

$$\begin{aligned} N_{\text{sources}}(\text{DM}, \delta) &\propto \iiint dV \\ &\propto \int_0^l \int_0^\delta \int_0^{2\pi} \rho^2 \sin \theta d\theta d\varphi d\rho \\ &\propto l^3 \cos(\delta) \\ &\propto \text{DM}^3 \cos(\delta), \end{aligned}$$

where l is the distance for which DM is a proxy.

4.3. *Detection probability vs DM and δ .* The probability of detecting the source as a function of DM and δ is complex because it relates to the observational realities of the telescope. We model three main contributing factors: the effects of (i) the telescope’s exposure, (ii) the fluence (defined below) distribution of FRBs, and (iii) the telescope’s sensitivity.

⁴This assumption is most appropriate for the very nearby, or low redshift, Universe. The repeater association significance is most complex in the high intensity regions of the NHPP, which happens to be near $\text{DM} \sim 500 \text{ pc cm}^{-3}$ (Macquart et al., 2020; James et al., 2022; Baptista et al., 2024), which is a reasonable place to make this assumption.

i) Exposure. The exposure at a declination is the amount of time that the telescope has collected data at that declination. At a fixed δ , CHIME observes some α span instantaneously, which can be described with an arclength on the celestial sphere. This arclength is roughly constant for all δ , forming a long (in the N-S direction) rectangle on the sky. Hence, given some exposure time proportional to the duration of the experiment, where that constant arclength subtends an α angle of 360 degrees (at δ near 90 degrees), each spot on the sky is seen for the duration of the experiment. For lower δ , this arclength subtends only a fraction of the circumference, and therefore exposure time on a source on that part of the sky is proportional to the fraction of the circumference that the arclength represents. The exposure for each source as a function of δ is thus proportional to $1/\cos(\delta)$. However, the experiment has been running for only a finite amount of time, so a function representing the exposure should not asymptote to infinity at $\delta = 90$ degrees. Instead, we model the exposure as a function of δ as

$$\text{exposure}(\delta) = \frac{c}{1 + d \cos(\delta)}$$

with c, d real positive constants. This function reaches a finite maximum value of c at $\delta = 90$ degrees and a non-zero minimum value of $c/(1 + d)$ at $\delta = 0$ degrees, while still scaling as $1/\cos(\delta)$. This function produces a good fit to the CHIME/FRB exposure data as a function of δ as released in the most recent catalog of repeater candidates from [CHIME/FRB Collaboration \(2023\)](#).

4.3.1. Fluence distribution. Fluence is defined as the amount of incident energy on the telescope. Fluence is also hence proportional to the time-integrated energy of the radio burst divided by the distance to the observer squared. The probability of detecting a radio burst falls off with the FRB fluence. For a standard candle luminosity distribution⁵ in Euclidean space, one expects the cumulative fluence distribution to be well described by a power-law with index $-3/2$, $\text{CDF}(F) \propto F^{-3/2}$ where F is the FRB fluence. This standard candle assumption is an oversimplification of the true fluence distribution that is nonetheless consistent mathematically with studies of CHIME/FRB's sample and hence we use this power-law index ([Shin et al., 2023](#)). However, and simply stated, intrinsic FRB energies do vary, and the farther the source, the smaller the fraction of the distribution of FRB burst energies that would be detectable by the telescope.

Beyond our descriptions of relative detectable samples as a function of DM and δ , we model the probability of detecting a given source as a negative exponential, as the detection probability is typically modeled as 'complete', and hence a steep fall off in probability with decreasing fluence is expected. Complete, in this context, means a burst with a given fluence would be detected with 100% probability if its position was being observed by the telescope at the time of the burst. The Gamma function model is reminiscent of canonical galaxy luminosity functions, which compare input luminosities to a characteristic luminosity (we will use a characteristic DM, DM^* , which controls the width of the DM density distribution, as well as a DM intercept parameter, DM_0 , which adjusts where the distribution reaches maximal density, in the following paragraph) and are modeled as a negative exponential ([Schechter, 1976](#)).

⁵A 'standard candle' in astronomy is a population of sources with a single intrinsic luminosity, and hence whose differing fluences reflect only their distances from Earth.

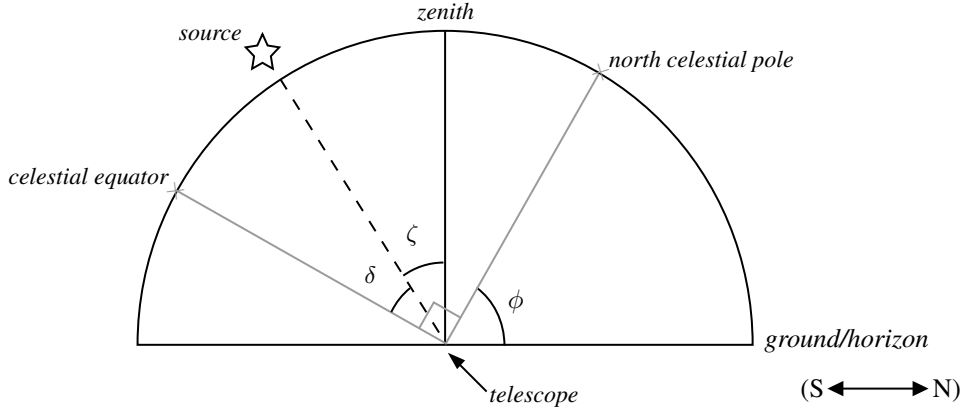


FIG 3. Illustration depicting the horizon-to-horizon view of the CHIME telescope to show the zenith angle (ζ) of a given source (indicated by a star) as a function of the declination of that source (δ). Zenith is defined as perpendicular to the horizon. The north celestial pole and celestial equator are defined as perpendicular to one another, and the north celestial pole is the axis around which the Earth spins. The angle between the north celestial pole and the horizon is equal to the geographic latitude (ϕ) of the telescope ($\phi \sim 49.32$ degrees (CHIME Collaboration, 2022)). The declination is defined as the angle between the source and the celestial equator. Hence we can calculate the zenith angle, ζ , of a source as $\zeta = \phi - \delta$.

4.3.2. *Sensitivity.* The sensitivity of a telescope describes the minimal brightness that the telescope can distinguish from random noise. The sensitivity of the CHIME telescope varies with location on the sky; CHIME is most sensitive directly overhead, at the telescope’s zenith, and the sensitivity decreases as a function of the zenith angle ζ (Figure 3).

Increased sensitivity means that a larger fraction of the luminosity function can be detected at a given distance, and thus one expects the DM with maximal probability of being detected to decrease as a function of increasing ζ . Therefore we modulate the term representing the maximal density DM, DM_0 , by a factor of $\cos(\zeta(\delta)) = \cos(\phi - \delta)$ where ϕ is the geographic latitude of the telescope (49.32 degrees, CHIME/FRB Collaboration 2018).

The global effect on the sensitivity as a function of δ can be described by $\cos^b(\zeta)$, where $b > 0$ is a constant, introduced to fit the steepness of the drop off in sensitivity with ζ . However, the way that CHIME/FRB forms beams on the sky means the sensitivity fluctuates around $\cos^b(\zeta)$ as a function of δ , with some positions falling in gaps between the most sensitive areas of each beam. Integrating over all observing frequencies and α , this effect is small compared to the sensitivity changes as a function of distance away from zenith, and median sensitivity is still well-described by $\cos^b(\zeta)$. Thus we do not model the small- δ -scale sensitivity behavior in the global intensity function, and instead rely on its imprint on the individual burst localization uncertainty regions, discussed in Section 4.4, to capture its contribution to the uncertainty in the posterior distributions. While we can make a reasonable estimate of b , (we know it will be greater than zero, and do not expect values much greater than 3 based on our beam model⁶), the exact value depends on how CHIME/FRB forms beams on the sky and the spectra and polarization of the observed FRBs, therefore we fit b rather than assert it in the intensity function (Noutsos et al., 2015; CHIME/FRB Collaboration, 2018).

We show the empirically estimated model of the telescope’s sensitivity as a function of δ in Figure 4 with a least squares fit to our model for this component, $\cos^b(\zeta)$ for illustrative purposes. There is a slight disagreement between the best-fit value $b = 1.45$ and the plotted sensitivity model, especially at low δ , but this disagreement will be reflected in the posterior

⁶available at <https://chime-frb-open-data.github.io/beam-model/>

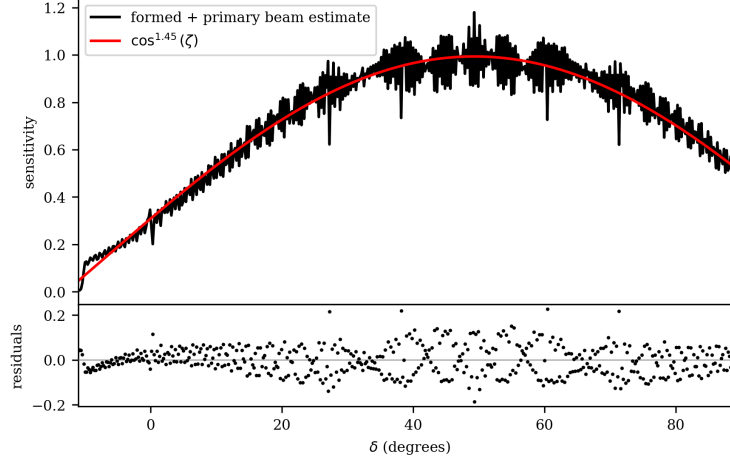


FIG 4. *top panel: Sensitivity as a function of declination and normalized to attain a max value at 1 at our zenith, intended to compare the behaviour of our best sensitivity estimate and $\cos^b(\zeta)$ (black line). The sensitivity estimate was modeled using CHIME/FRB’s publically available beam-model, available at <https://chime-frb-open-data.github.io/beam-model/>, by summing the two components of CHIME/FRB’s beam, the ‘formed’ beam and the ‘primary’ beam (a detailed description is more technical than appropriate to be included here, but can be found in CHIME/FRB Collaboration 2018). The sensitivity is expected to follow $\cos^b(\zeta)$ where b is a constant which depends on how CHIME/FRB forms beams on the sky as well as the polarization of FRBs (Noutsos et al., 2015; CHIME/FRB Collaboration, 2018). We use a simple least squares fit in order to estimate a value for b to show that the median of the sensitivity is well described by such a function. Bottom panel: residual values, i.e., $\cos^{1.45}(\zeta)$ model less the data from beam estimate.*

distribution of b and occurs at a low-intensity region where the repeater significance is least ambiguous.

The intensity function we use thus defined

$$(8) \quad \Lambda(\delta, \text{DM}) | N_{\text{FRBs}}, b, c, d, \text{DM}_0, \text{DM}^* \propto N_{\text{FRBs}} \exp\left(\frac{c}{1 + d \cos(\delta)} - \left(\frac{1}{\text{DM}^*} \left(\text{DM} + \frac{\text{DM}_0}{\cos^b(\phi - \delta)}\right)\right)^{3/2}\right) \cos(\delta) \left(\frac{1}{\text{DM}^*} \left(\text{DM} + \frac{\text{DM}_0}{\cos^b(\phi - \delta)}\right)\right)^3.$$

where we use \propto rather than an equality because the total intensity should integrate to the expected rate of FRBs, N_{FRBs} .

4.4. *Measurement Error.* Each CHIME/FRB burst detection has a unique localization p.d.f. (which describes the noise or measurement error) due to its beam configuration, described in detail in Section 3.1 of CHIME/FRB Collaboration (2021). CHIME/FRB’s real-time pipeline calculates the most likely positions on the sky for detected bursts using ratios among per beam signal-to-noise values fit to beam model predictions for a grid of model sky locations and model intrinsic spectra. The confidence interval map or distribution is estimated from a sample of events from radio transients with precisely known positions also detected by CHIME/FRB, such that true positions fall within contours of a given confidence interval with the appropriate frequency. CHIME/FRB’s primary beam sensitivity in the E–W direction, mostly concerning the α of sources, has roughly the form of a $\text{sinc}(x) \equiv \sin(x)/x$ function with origin at the meridian (directly overhead the telescope in the α plane) of the

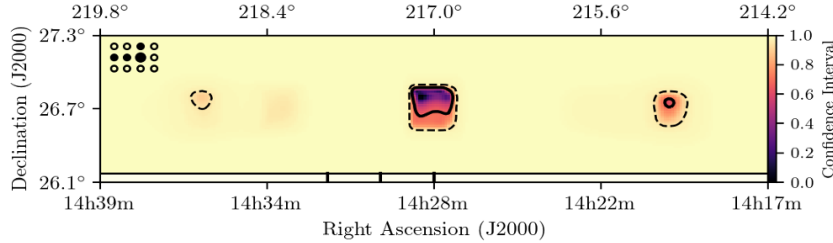


FIG 5. An example of uncertainty regions for FRB localizations with CHIME/FRB’s real-time pipeline, to demonstrate the multi-modal nature. The colormap shows which confidence interval percentage one would need to consider in order to include that position in the localization error. That is, the tan regions, or values near 1.0, are less likely to be the true position of the burst compared to the values near 0 (purple regions). In this plot, the unit for α is not fractional degrees but rather hours and minutes of arc, where 360 degrees are equal to 24 archours, and one degree is 60 arcminutes. The dots in the upper left corner illustrate the pattern of CHIME/FRB’s beams in which the burst was detected. Credit: CHIME/FRB Collaboration (2021).

telescope. The localization uncertainty regions reported are chosen to contain the ‘main lobe’ (or largest amplitude oscillation, using the sinc function analogy) of the primary beam and the first order ‘side lobes’ (the oscillations to the left and right of the largest amplitude of the sinc function) of the formed beams, which leads to multi-modal uncertainty regions. An example of these uncertainty regions is shown in Figure 5. We sample true positions from the uncertainty regions of each burst when estimating the posterior distributions of the intensity function.

4.5. *Putting it all together.* We take a Bayesian approach to fitting the model specified in Section 2 for the functional form of our application’s intensity function. We use a well-studied subset of FRBs, CHIME/FRBs first catalog (CHIME/FRB Collaboration, 2021), to sample the posterior distributions of the hyperparameters. This is done using a bespoke Metropolis-Hasting within block Gibbs sampler (see, e.g., Stenning and van Dyk, 2018, for a description using astrophysical examples). Our sampling algorithm is described in Algorithm 1.

Algorithm 1 MCMC sampling for generalized Hierarchical Bayesian Spatial Process

```

1: for  $i = 1 \rightarrow n$  samples: do
2:   block update from multivariate normal distribution of hyperparameters with Metropolis–Hastings (MH)
3:   for  $j = 1 \rightarrow \text{len}(\text{training data})$ : do
4:     block update for event positions  $(\alpha_j, \delta_j)$  with MH independence samples
5:   end for
6:   for  $j = 1 \rightarrow \text{len}(\text{training data})$ : do
7:     single-site update for burst DM with Metropolis sampler
8:   end for
9: end for
10: Iterate

```

Leveraging the posterior distributions of the hyperparameters, we can then make a predictive inference on the k -contact distance at a given α, δ , DM for the current CHIME/FRB experiment/current FRB detection count. We can quantify the probability of detecting k or more bursts within the observed distance of the minimal bounding sphere $(b(s_0, r) \subset D)$ or closer, under the null hypothesis that all bursts are physically independent.

Computational Specifics. To propose new values during each iteration of our MCMC routine, we use the following jumping distributions

$$(a_{i+1}, b_{i+1}, c_{i+1}, d_{i+1}, \text{DM}_{0,i+1}, \text{DM}^*_{i+1})^T \sim \mathcal{N}_5((a_i, b_i, c_i, d_i, \text{DM}_{0,i}, \text{DM}^*_{i})^T, \mathbb{M}_{ij}),$$

with a 6×6 real-valued, positive-semi-definite covariance matrix \mathbb{M}_{ij} estimated from the first 1000 iterations of an MCMC run, which are discarded as burn in and after which \mathbb{M}_{ij} remains fixed. For the block updates of α_i, δ_i , $i \in 1, 2, \dots, 526$, we use an independence sampler. This is a version of a Metropolis-Hastings sampler wherein the proposal distribution is random within the domain, weighted by an approximation of the posterior distribution (in our case, ε_i), and hence depending on the previous iteration only in the acceptance step of the algorithm. We weight according to an empirical estimate of the p.d.f. for the position of each burst (more information in Section 4.4). We do single-site Metropolis-Hastings updates for the DM of each burst using a Normal jumping distribution centered at the previous iteration value of the DM and with standard deviation equal to the estimated measurement standard deviation, typically between 0.4 to 3 pc cm⁻³, reflecting the telescope’s real-time pipeline measurement precision.

Hyperprior distribution. Our Bayesian approach to model fitting requires the specification of a prior distribution. We assume prior independence among the hyperparameters and specify the joint hyperprior distribution as the product of the following univariate distributions:

$$\begin{aligned} N_{\text{FRBs}} &\sim \text{Uniform}(128.8, 2362.8) & b &\sim \text{Normal}(1.45, 0.12) \\ \text{DM}_0 &\sim \text{Normal}(560, 560) & c &\sim \text{Uniform}(0, 10) \\ \text{DM}^* &\sim \text{Normal}(404, 404) & d &\sim \text{Uniform}(0, 10) \end{aligned}$$

We elicit the prior distribution on N_{FRBs} based on the known survey duration of 214.8 days (data not otherwise used in this work; CHIME/FRB Collaboration, 2021) and a pre-experiment estimate of CHIME/FRB’s detection rate of 0.6-11 bursts/day (CHIME/FRB Collaboration, 2018), which was calculated using the all-sky FRB rate from Lawrence et al. (2017) and adjusted for CHIME/FRB’s survey design by Chawla et al. (2017). N_{FRBs} can be any real number rather than only natural numbers as it is treated as the Poisson rate over the domain, where the likelihood in Equation 5 is computed as the likelihood of $n \in \mathbb{N}$ events in our sample given the overall rate of $N_{\text{FRBs}} \in \mathbb{R}$. The center and standard deviation of the Normal prior distribution of b is based on the best fit value and least squares error of fit to the beam model. Our distribution of DM_0 and DM^* are based on detected FRBs from surveys other than CHIME/FRB: we download all reported FRBs on the transient name server⁷ and exclude those detected by CHIME/FRB (our data). We then take the sample average and standard deviation of these non-CHIME/FRB FRB excess DMs, approximately 560 and 404 pc cm⁻³ respectively.

5. Performance.

5.1. *Convergence.* In addition to visual inspection of the chains and monitoring of acceptance rates throughout, we diagnose convergence using multiple chains with starting values chosen via latin hypercube sampling (McKay, Beckman and Conover, 1979).

In order to test that the results are insensitive to the choice of starting values for the MCMC routine, we run ten chains in total for which the starting values for each are determined as follows. For each hyperparameter, we select ten different starting values by dividing the

⁷<https://www.wis-tns.org/> accessed Aug 1st, 2024

marginal hyperprior into ten equal probability regions and selecting a random variate from each. Practically, we accomplish this by dividing the interval of reals $[0, 1)$ into sub-intervals $([0, 1/10), [1/10, 2/10), \dots, [9/10, 1))$, and picking a random value from each. Then, we take the corresponding value of the hyperparameter from the inverse cumulative distribution of the hyperprior. This process is repeated for each of the six hyperparameters. Then we sample randomly from the sets of each hyperparameter without replacement in order to select the vector of starting values for each chain. This ensures an even sampling from the hyperprior.

Visual inspection of the trace plots suggests that each chain converged to the same apparent stationary distribution. To further check convergence, we compute the Gelman and Rubin \hat{R} statistic (Gelman and Rubin, 1992) for each of the hyperparameters and find a maximum value of 1.00637, which does not indicate a lack of convergence. In addition, we compute the effective sample size of all ten chains using the `ArviZ` package⁸ (ArviZ Developers, 2020) and find no value smaller than 1514, which is more than sufficient for our purposes.

5.2. Simulation Study of Intensity function hyperparameters. In order to test the reliability of this methodology, we test an NHPP described by our intensity function with known hyperparameters, chosen to be $N_{\text{FRBs}}, b, c, d, \text{DM}_0, \text{DM}^*$ equal to 525, 1.5, 6, 2, 560, 400 respectively. These values are chosen as they are similar to the median hyperparameter values derived for our data. We randomly draw ten samples of events from this known intensity function by (i) drawing the number of observed events, with a Poisson distribution with rate equal to 525, (ii) selecting that number of positions from the known Λ using rejection sampling, and then (iii) perturbing these positions to simulate the noisy observations. We then run our MCMC method, outlined in Section 4.5, on the output noisy datasets. The chains are started at parameter values drawn from their hyperpriors using the same latin hypercube sampling technique as above: we divide the interval $(0,1)$ into 10 (number of chains) subintervals, randomly sample a value from those subintervals corresponding to each hyperparameter, and then draw the value of the starting hyperparameter from the icdf of it's marginal hyperprior. We then randomly permute these starting parameter values, without replacement. Since the covariance matrix we used to propose new values for the hyperparameters was tuned to the real dataset, we allow the chains to update the jumping distribution matrix M_{ij} to the chain's current covariance at iteration 1000 and remove all iterations before this as burn-in. We compare the posterior distributions to the known values and find that the true value of the $N_{\text{FRBs}}, b, c, d, \text{DM}_0, \text{DM}^*$ hyperparameter falls within the 90% credible interval of the estimated posterior distribution for 10, 10, 9, 8, 10, 10 simulations out of 10 total simulations, respectively, indicating that the method has good frequentist coverage for our intensity function.

6. Results.

6.1. Posterior distribution of the intensity hyperparameters. In Figure 6 we display a corner plot made from the MCMC samples. Using the sample median of the draws for each hyperparameter as an estimate of the posterior median, we show the corresponding median intensity in Figure 7 for illustrative purposes. In the marginals, we show the pointwise 90% credible region from all draws from the posterior distribution, as well as the pointwise median. We overlay the null data set detections to compare the realization of the intensity in the catalog/null dataset. While this intensity form is required in order to compute our motivating statistic, P_C , it also confirms that the instrument's intensity function is well-fit by a model based on known physics and spherical geometry. This is useful for studying the bias in CHIME/FRB detections, its affect on scientific results, and for modeling applications such as discussed by James (2023).

⁸version 1.2.0, <https://github.com/arviz-devs/arviz>

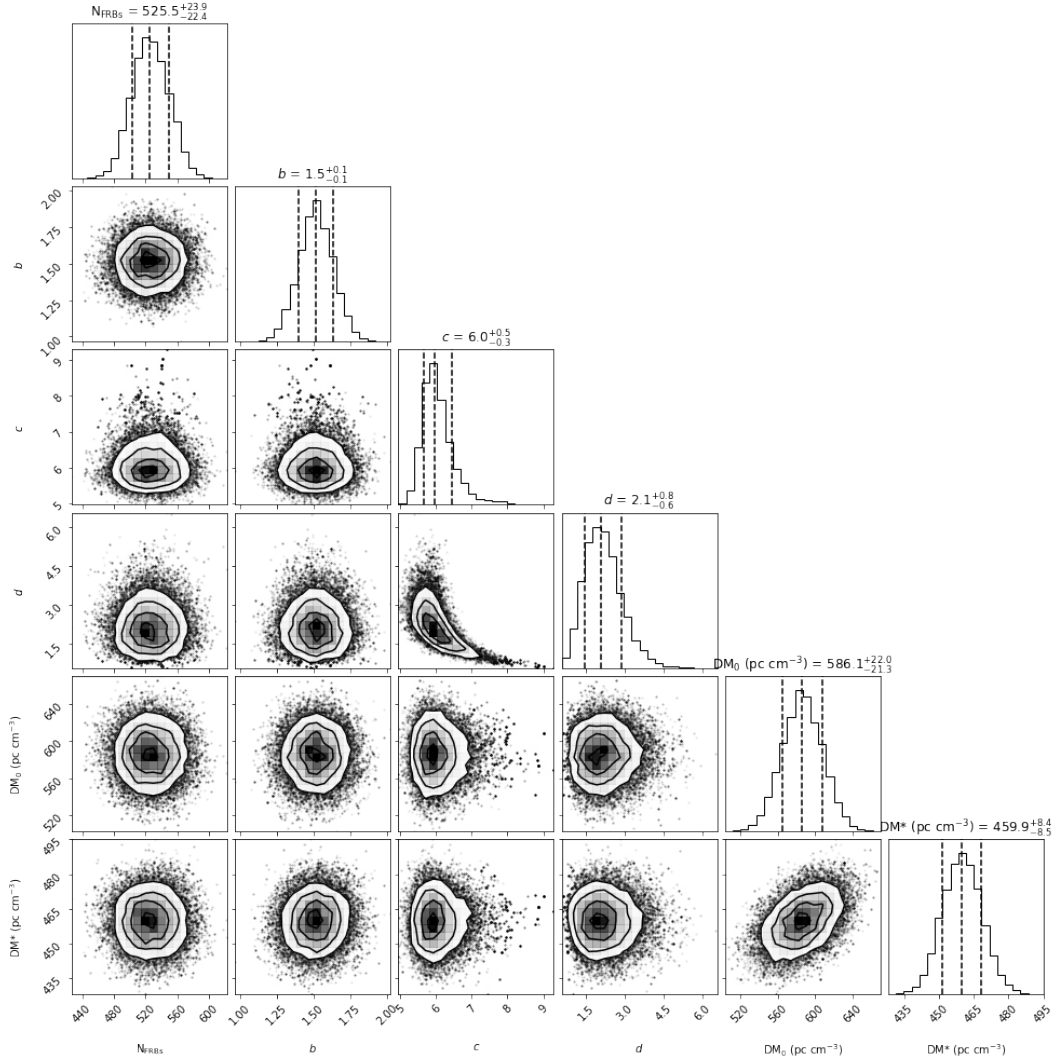


FIG 6. Corner plot of non-homogeneous spatial Poisson intensity hyperparameters from the (approximate) posterior draws obtained with MCMC. The values written in the titles of the histograms correspond to the median posterior distribution estimate for each parameter, and the errors represent the bounds of their 68% credible regions.

6.2. *CHIME/FRB Collaboration (2023) Repeater sample.* We estimate the P_C value for each of the repeater candidates of *CHIME/FRB Collaboration (2023)* both using the bound in Equation 7 and directly from simulations. The simulations sample true/unobserved positions from estimates of their error density distributions and then compute the probability in Equation 9. The bound in Equation 6 is an upper limit on the probability of a k -contact distance smaller than or equal to the observed value for each of the repeater candidates.

Both the probability and probability bound estimations require integration which is computed via Monte Carlo. Each random draw for the Monte Carlo integration uses a set of hyperparameters from our posterior distribution for Λ , but with N_{FRBs} multiplied by a factor which reflects the increased number of events in the training set versus observed events in the *CHIME/FRB Collaboration (2023)* dataset (i.e., 2196/526, the ratio of number of observed events in the repeater catalog to the number of observed events in the training data). The

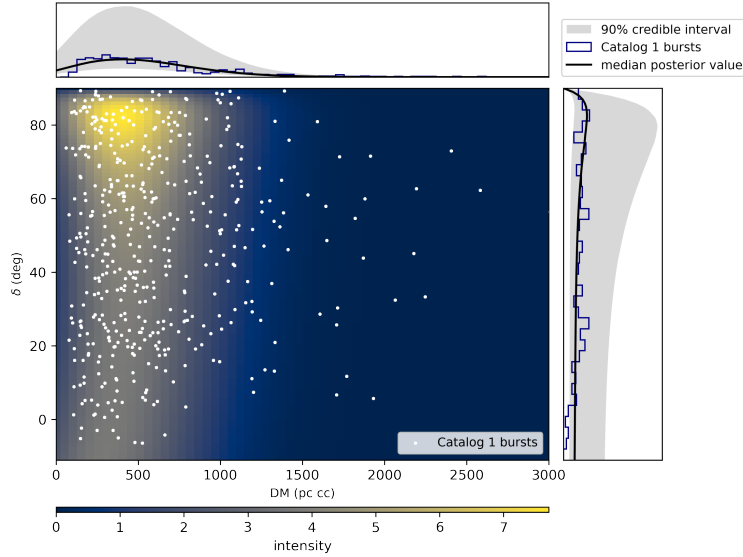


FIG 7. Center plot: CHIME/FRB intensity predicted from the median posterior hyperparameters. We overplot the FRB detections in the First CHIME/FRB catalog (CHIME/FRB Collaboration, 2021), our training set, as a function of δ and DM (white points). In the right and top subplots, we show a normalized histogram of these FRB detections (navy) as a function of δ and DM, respectively. In these panels, we also show the 90% pointwise credible interval (grey regions) and median point-wise value (black lines) from the posterior distribution.

observed value of the k -contact distance and the repeater’s observed position used in these methods are defined by estimating the minimal bounding sphere of the candidate repeater.

We estimate the minimal bounding sphere using the algorithm described in Chapter V.2 of Glassner (1990).

In Figure 8 the values are plotted against a modified value of the existing statistic for these sources, R_{CC} . R_{CC} estimates the false-positive contamination rate within the repeater sample (i.e., corrected for multiple-hypothesis testing) assuming each FRB detection is an independent binomial trial, where a ‘success’ is a detection within some box around the repeater candidate, and a ‘failure’ is a detection outside. We multiply these R_{CC} values by the trials factor such that the values can be considered a probability of coincidence and can be directly compared with our P_C estimates, and plot this value R_{CC}/N denoted P_C (previous work). The intensity function of CHIME/FRB Collaboration (2023) is estimated by smoothing the two dimensional detection histogram with a Gaussian kernel, and the probability of success/failure is approximated as the fraction of intensity inside/outside of the box. The main issues with this method are the ambiguity of defining the ‘in’ box, and that it does not take into account measurement error other than the 95% span of the localization and DM errors, inside of which all possibilities are equally weighted despite the multi-modal nature of the error regions. The intensity function also doesn’t properly account for measurement error, and the choice of Gaussian kernel could potentially obscure minute fluctuations in intensity, or could overweight a stochastic over- or under- density.

In 32 of 37 cases, our new methodology returns a smaller median P_C for the repeater candidate, meaning the candidates are considered less likely to be independent sources, with a median improvement factor (original P_C / our P_C estimate) of over 3000. This includes 13 candidates that were previously labeled as ambiguous due to their high P_C , whereas the new methodology produces values of P_C that suggest that the sources are unambiguously repeaters (assuming the same p -value threshold as adapted by CHIME/FRB Collaboration 2023). In two of 37 cases, the returned estimated probability is zero, reflecting that

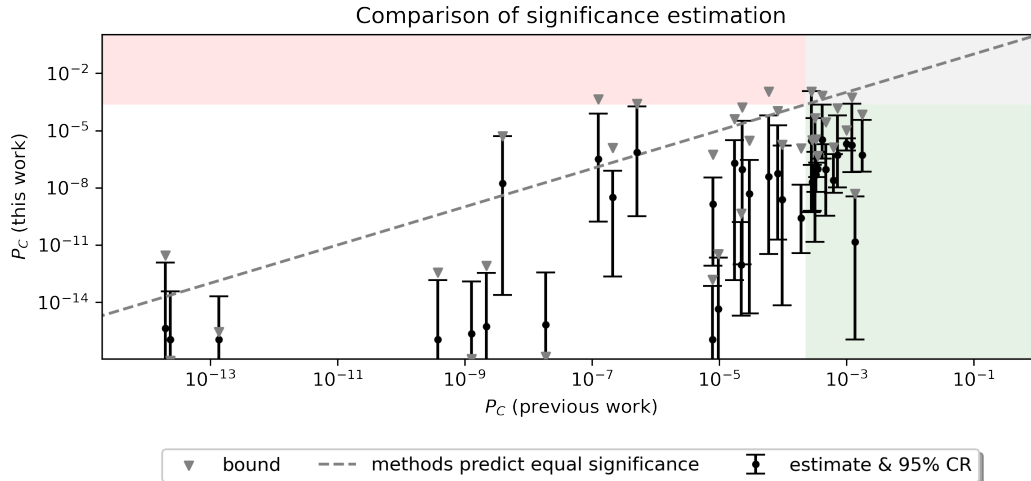


FIG 8. Comparison of probability of coincidence (P_C) from the previous method (x -axis) and from the method derived in this work (y -axis) for repeater candidates from [CHIME/FRB Collaboration \(2023\)](#). This work presents both a probability estimate from simulations (black points, errorbars represent the 95% credible region) and a probability bound estimate (grey triangles). We denote the line at which the estimates from the new and old methods would be equal with a gray dotted line. Candidates in the unshaded plot region would be classified as having sufficient evidence to call the source a repeater in both methods, and candidates in the grey shaded region have P_C estimates from both methods that would suggest the candidates are ambiguous. The thirteen candidates in the green region are candidates that can be newly declared unambiguous repeater candidates using the P_C method outlined in this paper. In 32 of 37 cases, the new method returns a decreased P_C for the repeater candidate, with a median ratio between the old and new P_C estimates on the order of 3000, suggesting improved sensitivity from the updated model.

the estimate is smaller than can be accurately captured by our double-precision floating-point format (roughly 10^{-16}). This conclusion is supported by the estimate of the upper bound probabilities for these sources, 3×10^{-18} and 1×10^{-17} . Our Bayesian methodology allows for uncertainty quantification in the estimate. In the direct simulation of P_C we randomly sample true positions from the localization distributions and randomly sample $\theta = \{N_{\text{FRBs}}, b, c, d, \text{DM}_0, \text{DM}^*\}$ for Λ from our estimate of its posterior distribution. We then compute the probability in Equation 9 assuming these true positions and this set of hyperparameters and repeat 5000 times. The 95% credible regions on the value of P_C from this method are also shown in Figure 8. Considering the credible regions, it is clear that the P_C estimates tend to be lower than the P_C (previous work) value. For the repeater candidates whose median simulated value of P_C are lower than the threshold p -value in [CHIME/FRB Collaboration \(2023\)](#), the span of the 95% credible region tends to be entirely below this threshold p -value. The width of the 95% credible regions are also similar in magnitude to the difference between the median value of P_C estimated from direct simulation and the upper bound on P_C from Equation 7. This is promising for high-dimensional applications which would benefit from the decreased computational cost of the bound. The improvement in the majority of cases by large factors suggests that this method is more sensitive and hence can result in the identification of more repeaters.

6.3. *Limitations.* As discussed in Section 4, a complicating factor is the acquisition of a proper null data set consisting of unique FRB sources detected by CHIME/FRB. The repeat bursts cannot be unambiguously removed from the sample without the results of the test

for which we need the data set. However, the inclusion of repeat bursts artificially increases the intensity of the NHPP in that area and overall, making the test less likely to identify a repeater, considered conservative in this application.

7. Conclusions. While much thought has gone into the treatment of nonhomogeneous Poisson processes (NHPP) observed with noise, second order characteristics of these processes had previously not been studied, since the noisy process is not typically the process of interest. In this paper, we use noisy data in a hierarchical Bayesian model to fit hyperparameters of a physically motivated nonhomogeneous Poisson process intensity. In simulation studies, we find that this methodology leads to reliable estimates of the true values of these hyperparameters. We then use the posterior distribution to make an inference on the noisy non-homogeneous Poisson process, the probability of detecting k events within some radius r and center point in the domain.

When applied to our motivating application, the new methodology for computing probability of coincidence increases the significance of candidate repeaters previously reported in [CHIME/FRB Collaboration \(2023\)](#) 86% of the time, with a median improvement factor on the order of 3000.

Our methodology has been adapted by the CHIME/FRB collaboration and will be used to define the sample for an upcoming fourth catalog of repeaters from CHIME/FRB. With an additional two years worth of data (compared to [CHIME/FRB Collaboration 2023](#)) and the increased sensitivity offered from this methodology, the catalog is expected to roughly double the number of known repeaters.

More generally, in the field of FRBs, our methodology has consequences for not only for associations between FRBs (repeaters), but also between FRBs and other events (such as gravitational wave sources). Unambiguous classifications in these cases are vital, as increasing the repeater sample size and detecting outlier repeaters (which, for example, could be the most promising for follow-up or otherwise particularly interesting astrophysically) can give us insight into the progenitors of FRBs and the relationship between observational subclasses of FRBs. Similarly, associations between FRBs and other poorly localized transients, like gravitational wave events, which have known progenitors, could result in a field-changing discovery.

While this methodology is geared towards astrophysical observations with significant localization uncertainty, the common application of NHPPs to fields like ecology and epidemiology suggests that the method may be beneficial for research in other disciplines, for example, hotspot detection.

APPENDIX A: PROBABILITY OF A CLUSTER OF K EVENTS

THEOREM 1. ([Berman, 1977](#)) *If X is a uniform Poisson point process in \mathbb{R}^d of intensity Λ , $d_k(s_0, X)$ for $s_0 \in \mathbb{R}^d$ denotes the distance from s_0 to the k^{th} nearest point in X , the distribution function of $d_k(s_0, X)$ is:*

$$(9) \quad Pr(d_k(s_0, X) < r) = 1 - \sum_{i=1}^{k-1} \frac{\left(\int_{B(u,r)} \Lambda(s) ds\right)^i}{i!} e^{-\int_{B(u,r)} \Lambda(s) ds}$$

where $B(u, r)$ is the closed d -ball centered at $u \in \mathbb{R}^d$ with radius r

PROPOSITION 1. *Suppose $\mathbf{X} = \{\mathbf{x}_1, \dots, \mathbf{x}_n\} \subseteq D \subseteq \mathbb{R}^d$ is a nonhomogeneous Poisson point process with intensity $\Lambda(s)$. D is the observation window/domain and we assume that $\Lambda(\mathbf{s}) = 0$ for $\mathbf{s} \notin D$. Let $\mathbf{Y} = \{\mathbf{y}_1, \dots, \mathbf{y}_n\}$ be the point process of the noisy event locations where $\mathbf{y}_i = \mathbf{x}_i + \boldsymbol{\varepsilon}_i$. $\boldsymbol{\varepsilon}_i$ is a random vector in \mathbb{R}^d that describes the spatial uncertainty of*

the true event location \mathbf{x}_i . We assume that $\{\varepsilon_i\}_{i=1}^n$ are independent of each other and \mathbf{X} . We further assume that D and ε_i 's are such that $\mathbf{y}_i \notin D$ with probability zero so that $\mathbf{Y} \subseteq D$ a.s. The distribution function of the distance from $s_0 \in D$ to the k -th nearest point in \mathbf{Y} is bounded by

$$P(d_k(s_0, \mathbf{Y}) \leq r) \leq \int_{\text{supp}(\varepsilon_1)} \cdots \int_{\text{supp}(\varepsilon_k)} \left\{ 1 - \sum_{i=0}^{k-1} \frac{\left(\int_{B(s_0, \tilde{r})} \Lambda(s) \mu(ds) \right)^i}{i!} \times \right. \\ \left. \exp \left(- \int_{B(s_0, \tilde{r})} \Lambda(s) \mu(ds) \right) \right\} f(\{\varepsilon_i\}_{i=1}^k) \mu(d\varepsilon_1) \cdots \mu(d\varepsilon_k)$$

where $\tilde{r} = r + \max\{|\varepsilon_i| : 1 \leq i \leq k\}$ and $f(\{\varepsilon_i\}_{i=1}^k)$ is the joint p.d.f. of $\{\varepsilon_i\}_{i=1}^k$. The support of ε_i is denoted $\text{supp}(\varepsilon_i)$ and μ is the Lebesgue measure.

If the ε_i are i.i.d., the above can be further simplified to

$$P(d_k(s_0, \mathbf{Y}) \leq r) \leq \int_0^\infty \left\{ 1 - \sum_{i=0}^{k-1} \frac{\left(\int_{B(s_0, r+x)} \Lambda(s) \mu(ds) \right)^i}{i!} \times \right. \\ \left. \exp \left(- \int_{B(s_0, r+x)} \Lambda(s) \mu(ds) \right) \right\} k f_d^{k-1}(x) dx,$$

where $k f_{|\varepsilon_i|}^{k-1}(x)$ is the p.d.f. of $\max\{|\varepsilon_i| : 1 \leq i \leq k\}$

PROOF. $\{d_k(s_0, \mathbf{Y}) \leq r\}$ is equivalent to $\{N[\mathbf{Y} \cap B(s_0, r)] \geq k\}$, where $N(\mathbf{Y} \cap A)$ is the number of events from \mathbf{Y} in the set A . Thus

$$P(d_k(s_0, \mathbf{Y}) \leq r) = P(N[\mathbf{Y} \cap B(s_0, r)] \geq k).$$

Denote the set of points $\{\mathbf{Y} \cap B(s_0, r)\} = \{\mathbf{y}_1, \dots, \mathbf{y}_{n_r}\} = \{\mathbf{x}_1 + \varepsilon_1, \dots, \mathbf{x}_{n_r} + \varepsilon_{n_r}\}$. Note that n_r here is random and the indices $1 \leq i \leq n_r$ for \mathbf{x}_i 's and ε_i 's are permutation invariant. Clearly,

$$\{N[\mathbf{Y} \cap B(s_0, r)] \geq k\} = \{\{\mathbf{x}_1 + \varepsilon_1, \dots, \mathbf{x}_{n_r} + \varepsilon_{n_r}\} \subset B(s_0, r) \text{ and } n_r \geq k\}.$$

Without loss of generality, we can condition on $\{\varepsilon_i\}_{i=1}^k$, and write $B(s_0, \tilde{r}) = B(s_0, r + \max\{|\varepsilon_i| : 1 \leq i \leq k\})$. Hence, $\{\mathbf{x}_1 + \varepsilon_1, \dots, \mathbf{x}_{n_r} + \varepsilon_{n_r}\} \subset B(s_0, r)$ and $n_r \geq k$ implies that at least $\{\mathbf{x}_1, \dots, \mathbf{x}_k\} \subseteq B(s_0, \tilde{r})$ and thus $N[\mathbf{X} \cap B(s_0, \tilde{r})] \geq k$. Therefore,

$$P(N\{\mathbf{Y} \cap B(s_0, r)\} \geq k \mid \{\varepsilon_i\}_{i=1}^k) \leq P(N\{\mathbf{X} \cap B(s_0, \tilde{r})\} \geq k \mid \{\varepsilon_i\}_{i=1}^k) \\ = 1 - P(N\{\mathbf{X} \cap B(s_0, \tilde{r})\} \leq k-1 \mid \{\varepsilon_i\}_{i=1}^k).$$

By the law of total probability and Theorem 1, we have

$$P(N\{\mathbf{Y} \cap B(s_0, r)\} \geq k) = \int_{\text{supp}(\varepsilon_1)} \cdots \int_{\text{supp}(\varepsilon_k)} P(N\{\mathbf{Y} \cap B(s_0, r)\} \geq k \mid \{\varepsilon_i\}_{i=1}^k) \times \\ f(\{\varepsilon_i\}_{i=1}^k) \mu(d\varepsilon_1) \cdots \mu(d\varepsilon_k) \\ \leq \int_{\text{supp}(\varepsilon_1)} \cdots \int_{\text{supp}(\varepsilon_k)} \left\{ 1 - P(N\{\mathbf{X} \cap B(s_0, \tilde{r})\} \leq k-1 \mid \{\varepsilon_i\}_{i=1}^k) \right\} \times \\ f(\{\varepsilon_i\}_{i=1}^k) \mu(d\varepsilon_1) \cdots \mu(d\varepsilon_k)$$

$$\leq \int_{\text{supp}(\varepsilon_1)} \cdots \int_{\text{supp}(\varepsilon_k)} \left\{ 1 - \sum_{i=0}^{k-1} \frac{\left(\int_{B(s_0, \bar{r})} \Lambda(s) \mu(ds) \right)^i}{i!} \times \right. \\ \left. \exp \left(- \int_{B(s_0, \bar{r})} \Lambda(s) \mu(ds) \right) \right\} f(\{\varepsilon_i\}_{i=1}^k) \mu(d\varepsilon_1) \cdots \mu(d\varepsilon_k).$$

Suppose ε_i are i.i.d., and $f_{|\varepsilon_i|}(x)$ is the p.d.f. of $|\varepsilon_i|$. Then the k -dimensional integral in the last line above with respect to $\{\varepsilon_i\}_{i=1}^k$ can be substituted by the one-dimensional integral with respect to $x = \max\{|\varepsilon_i| : 1 \leq i \leq k\}$. Thus,

$$P(d_k(s_0, \mathbf{Y}) \leq r) \leq \int_0^\infty \left\{ 1 - \sum_{i=0}^{k-1} \frac{\left(\int_{B(s_0, r+x)} \Lambda(s) \mu(ds) \right)^i}{i!} \times \right. \\ \left. \exp \left(- \int_{B(s_0, r+x)} \Lambda(s) \mu(ds) \right) \right\} k f_{|\varepsilon_i|}^{k-1}(x) dx,$$

where $k f_{|\varepsilon_i|}^{k-1}(x)$ is the p.d.f. of $\max\{|\varepsilon_i| : 1 \leq i \leq k\}$. \square

Acknowledgments. We acknowledge that CHIME is located on the traditional, ancestral, and unceded territory of the Syilx/Okanagan people. We are grateful to the staff of the Dominion Radio Astrophysical Observatory, which is operated by the National Research Council of Canada.

Funding. This work was funded in large part by a Canadian Statistical Sciences Institute (CANSSI) Collaborative Research Team Grant to author G.M.E.. CANSSI is supported under the Discovery Institutes Support program of the Natural Sciences and Engineering Research Council of Canada (NSERC). A.M.C. is funded by an NSERC Doctoral Postgraduate Scholarship. D.L. acknowledges support from the Data Sciences Institute Doctoral Fellowship at the University of Toronto, and from CANSSI Ontario Multi-disciplinary Doctoral Trainee Program. D.C.S. acknowledges the support of NSERC, RGPIN-2021-03985. The Dunlap Institute is funded through an endowment established by the David Dunlap family and the University of Toronto. B.M.G. acknowledges the support of NSERC through grant RGPIN-2022-03163, and of the Canada Research Chairs program. Z.P. is supported by an NWO Veni fellowship (VI.Veni.222.295). A.P. is funded by the NSERC Canada Graduate Scholarships – Doctoral program. A.B.P. is a Banting Fellow, a McGill Space Institute (MSI) Fellow, and a Fonds de Recherche du Québec – Nature et Technologies (FRQNT) postdoctoral fellow. J.X.P. acknowledges support from NSF grants AST-1911140, AST-1910471, and AST-2206490 as a member of the Fast and Fortunate for FRB Follow-up team. CHIME is funded by a grant from the Canada Foundation for Innovation (CFI) 2012 Leading Edge Fund (Project 31170) and by contributions from the provinces of British Columbia, Québec and Ontario. The CHIME/FRB Project is funded by a grant from the CFI 2015 Innovation Fund (Project 33213) and by contributions from the provinces of British Columbia and Québec, and by the Dunlap Institute for Astronomy and Astrophysics at the University of Toronto. Additional support was provided by the Canadian Institute for Advanced Research (CIFAR), McGill University and the Trottier Space Institute thanks to the Trottier Family Foundation, and the University of British Columbia.

REFERENCES

- AGGARWAL, K., BUDAVÁRI, T., DELLER, A. T., EFTEKHARI, T., JAMES, C. W., PROCHASKA, J. X. and TENDULKAR, S. P. (2021). Probabilistic Association of Transients to their Hosts (PATH). *ApJ* **911** 95. <https://doi.org/10.3847/1538-4357/abe8d2>

- BAPTISTA, J., PROCHASKA, J. X., MANNINGS, A. G., JAMES, C. W., SHANNON, R. M., RYDER, S. D., DELLER, A. T., SCOTT, D. R., GLOWACKI, M. and TEJOS, N. (2024). Measuring the Variance of the Macquart Relation in Redshift–Extragalactic Dispersion Measure Modeling. *ApJ* **965** 57. <https://doi.org/10.3847/1538-4357/ad2705>
- BAR-HEN, A., CHADŒUF, J., DESSARD, H. and MONESTIEZ, P. (2013). Estimating second order characteristics of point processes with known independent noise. *Statistics and Computing* **23** 297–309. <https://doi.org/10.1007/s11222-011-9311-7>
- BECKWITH, S. V. W., STIAVELLI, M., KOEKEMOER, A. M., CALDWELL, J. A. R., FERGUSON, H. C., HOOK, R., LUCAS, R. A., BERGERON, L. E., CORBIN, M., JOGEE, S., PANAGIA, N., ROBERTO, M., ROYLE, P., SOMERVILLE, R. S. and SOSEY, M. (2006). The Hubble Ultra Deep Field. *AJ* **132** 1729–1755. <https://doi.org/10.1086/507302>
- BERMAN, M. (1977). Distance Distributions Associated with Poisson Processes of Geometric Figures. *Journal of Applied Probability* **14**. <https://doi.org/10.2307/3213273>
- CHAKRABORTY, A. and GELFAND, A. E. (2010). Analyzing spatial point patterns subject to measurement error. *Bayesian Analysis* **5** 97–122. <https://doi.org/10.1214/10-ba504>
- CHAWLA, P., KASPI, V. M., JOSEPHY, A., RAJWADE, K. M., LORIMER, D. R., ARCHIBALD, A. M., DECESAR, M. E., HESSELS, J. W. T., KAPLAN, D. L., KARAKO-ARGAMAN, C., KONDRATIEV, V. I., LEVIN, L., LYNCH, R. S., MCLAUGHLIN, M. A., RANSOM, S. M., ROBERTS, M. S. E., STAIRS, I. H., STOVALL, K., SWIGGUM, J. K. and VAN LEEUWEN, J. (2017). A Search for Fast Radio Bursts with the GBNCC Pulsar Survey. *ApJ* **844** 140. <https://doi.org/10.3847/1538-4357/aa7d57>
- CHIME/FRB COLLABORATION (2018). The CHIME Fast Radio Burst Project: System Overview. *ApJ* **863** 48. <https://doi.org/10.3847/1538-4357/aad188>
- CHIME/FRB COLLABORATION (2019a). A second source of repeating fast radio bursts. *Nature* **566** 235–238. <https://doi.org/10.1038/s41586-018-0864-x>
- CHIME/FRB COLLABORATION (2019b). CHIME/FRB Discovery of Eight New Repeating Fast Radio Burst Sources. *ApJ* **885** L24. <https://doi.org/10.3847/2041-8213/ab4a80>
- CHIME/FRB COLLABORATION (2021). The First CHIME/FRB Fast Radio Burst Catalog. *ApJS* **257** 59. <https://doi.org/10.3847/1538-4365/ac33ab>
- CHIME COLLABORATION (2022). An Overview of CHIME, the Canadian Hydrogen Intensity Mapping Experiment. *ApJS* **261** 29. <https://doi.org/10.3847/1538-4365/ac6fd9>
- CHIME/FRB COLLABORATION (2023). CHIME/FRB Discovery of 25 Repeating Fast Radio Burst Sources. *ApJ* **947** 83. <https://doi.org/10.3847/1538-4357/acc6c1>
- COOK, A. M., BHARDWAJ, M., GAENSLER, B. M., SCHOLZ, P., EADIE, G. M., HILL, A. S., KASPI, V. M., MASUI, K. W., CURTIN, A. P., DONG, F. A., FONSECA, E., HERRERA-MARTIN, A., KACZMAREK, J., LANMAN, A. E., LAZDA, M., LEUNG, C., MEYERS, B. W., MICHILLI, D., PANDHI, A., PEARLMAN, A. B., PLEUNIS, Z., RANSOM, S., RAHMAN, M., SAND, K. R., SHIN, K., SMITH, K., STAIRS, I. and STENNING, D. C. (2023). An FRB Sent Me a DM: Constraining the Electron Column of the Milky Way Halo with Fast Radio Burst Dispersion Measures from CHIME/FRB. *ApJ* **946** 58. <https://doi.org/10.3847/1538-4357/acbbd0>
- CORDES, J. M. and LAZIO, T. J. W. (2002). NE2001.I. A New Model for the Galactic Distribution of Free Electrons and its Fluctuations. *arXiv e-prints astro-ph/0207156*. <https://doi.org/10.48550/arXiv.astro-ph/0207156>
- CUCALA, L. (2008). Intensity Estimation for Spatial Point Processes Observed with Noise. *Scandinavian Journal of Statistics* **35** 322–334.
- CURTIN, A. P., SIROTA, S., KASPI, V. M., TENDULKAR, S. P., BHARDWAJ, M., COOK, A. M., FONG, W.-F., GAENSLER, B. M., MAIN, R. A., MASUI, K. W., MICHILLI, D., PANDHI, A., PEARLMAN, A. B., SCHOLZ, P. and SHIN, K. (2024). Constraining Near-simultaneous Radio Emission from Short Gamma-Ray Bursts Using CHIME/FRB. *ApJ* **972** 125. <https://doi.org/10.3847/1538-4357/ad5c65>
- ARViZ DEVELOPERS (2020). ArviZ: Exploratory analysis of Bayesian models. Astrophysics Source Code Library, record ascl:2004.012.
- DOLAG, K., GAENSLER, B. M., BECK, A. M. and BECK, M. C. (2015). Constraints on the distribution and energetics of fast radio bursts using cosmological hydrodynamic simulations. *MNRAS* **451** 4277–4289. <https://doi.org/10.1093/mnras/stv1190>
- FONSECA, E., ANDERSEN, B. C., BHARDWAJ, M., CHAWLA, P., GOOD, D. C., JOSEPHY, A., KASPI, V. M., MASUI, K. W., MCKINVEN, R., MICHILLI, D., PLEUNIS, Z., SHIN, K., TENDULKAR, S. P., BANDURA, K. M., BOYLE, P. J., BRAR, C., CASSANELLI, T., CUBRANIC, D., DOBBS, M., DONG, F. Q., GAENSLER, B. M., HINSHAW, G., LANDECKER, T. L., LEUNG, C., LI, D. Z., LIN, H. H., MENAPARRA, J., MERRYFIELD, M., NAIDU, A., NG, C., PATEL, C., PEN, U., RAFIEI-RAVANDI, M., RAHMAN, M., RANSOM, S. M., SCHOLZ, P., SMITH, K. M., STAIRS, I. H., VANDERLINDE, K., YADAV, P. and ZWANIGA, A. V. (2020). Nine New Repeating Fast Radio Burst Sources from CHIME/FRB. *ApJ* **891** L6. <https://doi.org/10.3847/2041-8213/ab7208>

- GELMAN, A. and RUBIN, D. B. (1992). Inference from Iterative Simulation Using Multiple Sequences. *Statistical Science* **7** 457 – 472. <https://doi.org/10.1214/ss/1177011136>
- GLASSNER, A. S. (1990). *Graphics Gems. Graphics Gems - IBM*. Elsevier Science.
- JAMES, C. W. (2023). Modelling repetition in zDM: A single population of repeating fast radio bursts can explain CHIME data. *PASA* **40** e057. <https://doi.org/10.1017/pasa.2023.51>
- JAMES, C. W., PROCHASKA, J. X., MACQUART, J. P., NORTH-HICKEY, F. O., BANNISTER, K. W. and DUNNING, A. (2022). The z-DM distribution of fast radio bursts. *MNRAS* **509** 4775–4802. <https://doi.org/10.1093/mnras/stab3051>
- KIRSTEN, F., OULD-BOUKATTINE, O. S., HERRMANN, W., GAWROŃSKI, M. P., HESSELS, J. W. T., LU, W., SNELDERS, M. P., CHAWLA, P., YANG, J., BLAAUW, R., NIMMO, K., PUCHALSKA, W., WOLAK, P. and VAN RUITEN, R. (2024). A link between repeating and non-repeating fast radio bursts through their energy distributions. *Nature Astronomy* **8** 337–346. <https://doi.org/10.1038/s41550-023-02153-z>
- KOTTAS, A. and SANSÓ, B. (2007). Bayesian mixture modeling for spatial Poisson process intensities, with applications to extreme value analysis. *Journal of Statistical Planning and Inference* **137** 3151–3163. Special Issue: Bayesian Inference for Stochastic Processes. <https://doi.org/10.1016/j.jspi.2006.05.022>
- LANMAN, A. E., ANDREW, S., LAZDA, M., SHAH, V., AMIRI, M., BALASUBRAMANIAN, A., BANDURA, K., BOYLE, P. J., BRAR, C., CARLSON, M., CLICHE, J.-F., GUSINSKAIA, N., HENDRICKSEN, I. T., KACZMAREK, J. F., LANDECKER, T., LEUNG, C., MCKINVEN, R., MENA-PARRA, J., MILUTINOVIC, N., NIMMO, K., PEARLMAN, A. B., RENARD, A., RAHMAN, M., SHAW, J. R., SIEGEL, S. R., SMEGAL, R. J., CASSANELLI, T., CHATTERJEE, S., CURTIN, A. P., DOBBS, M., DONG, F. A., HALPERN, M., HOPKINS, H., KASPI, V. M., KHAIRY, K., MASUI, K. W., MEYERS, B. W., MICHILLI, D., PETROFF, E., PINSONNEAULT-MAROTTE, T., PLEUNIS, Z., RAFIEI-RAVANDI, M., SHIN, K., SMITH, K., VANDERLINDE, K. and ZEGMOTT, T. J. (2024). CHIME/FRB Outriggers: KKO Station System and Commissioning Results. *arXiv e-prints* arXiv:2402.07898. <https://doi.org/10.48550/arXiv.2402.07898>
- LAWRENCE, E., VANDER WIEL, S., LAW, C., BURKE SPOLAOR, S. and BOWER, G. C. (2017). The Nonhomogeneous Poisson Process for Fast Radio Burst Rates. *AJ* **154** 117. <https://doi.org/10.3847/1538-3881/aa844e>
- LI, D., WANG, P., ZHU, W. W., ZHANG, B., ZHANG, X. X., DUAN, R., ZHANG, Y. K., FENG, Y., TANG, N. Y., CHATTERJEE, S., CORDES, J. M., CRUCES, M., DAI, S., GAJJAR, V., HOBBS, G., JIN, C., KRAMER, M., LORIMER, D. R., MIAO, C. C., NIU, C. H., NIU, J. R., PAN, Z. C., QIAN, L., SPITLER, L., WERTHIMER, D., ZHANG, G. Q., WANG, F. Y., XIE, X. Y., YUE, Y. L., ZHANG, L., ZHI, Q. J. and ZHU, Y. (2021). A bimodal burst energy distribution of a repeating fast radio burst source. *Nature* **598** 267–271. <https://doi.org/10.1038/s41586-021-03878-5>
- LUND, J., PENTTINEN, A. and RUDEMO, M. (1999). Bayesian analysis of spatial point patterns from noisy observations, PhD thesis, Department of Mathematics and Physics, The Royal Veterinary and Agricultural University, Copenhagen.
- MACQUART, J. P., PROCHASKA, J. X., MCQUINN, M., BANNISTER, K. W., BHANDARI, S., DAY, C. K., DELLER, A. T., EKERS, R. D., JAMES, C. W., MARNOCH, L., OSŁOWSKI, S., PHILLIPS, C., RYDER, S. D., SCOTT, D. R., SHANNON, R. M. and TEJOS, N. (2020). A census of baryons in the Universe from localized fast radio bursts. *Nature* **581** 391–395. <https://doi.org/10.1038/s41586-020-2300-2>
- MCKAY, M. D., BECKMAN, R. J. and CONOVER, W. J. (1979). A Comparison of Three Methods for Selecting Values of Input Variables in the Analysis of Output from a Computer Code. *Technometrics* **21** 239–245.
- MOROIANU, A., WEN, L., JAMES, C. W., AI, S., KOVALAM, M., PANTHER, F. H. and ZHANG, B. (2023). An assessment of the association between a fast radio burst and binary neutron star merger. *Nature Astronomy* **7** 579–589. <https://doi.org/10.1038/s41550-023-01917-x>
- NIU, C. H., AGGARWAL, K., LI, D., ZHANG, X., CHATTERJEE, S., TSAI, C. W., YU, W., LAW, C. J., BURKE-SPOLAOR, S., CORDES, J. M., ZHANG, Y. K., OCKER, S. K., YAO, J. M., WANG, P., FENG, Y., NIINO, Y., BOCHENEK, C., CRUCES, M., CONNOR, L., JIANG, J. A., DAI, S., LUO, R., LI, G. D., MIAO, C. C., NIU, J. R., ANNA-THOMAS, R., SYDNOR, J., STERN, D., WANG, W. Y., YUAN, M., YUE, Y. L., ZHOU, D. J., YAN, Z., ZHU, W. W. and ZHANG, B. (2022). A repeating fast radio burst associated with a persistent radio source. *Nature* **606** 873–877. <https://doi.org/10.1038/s41586-022-04755-5>
- NOUSOS, A., SOBEY, C., KONDRATIEV, V. I., WELTEVREDE, P., VERBIEST, J. P. W., KARASTERGIOU, A., KRAMER, M., KUNIYOSHI, M., ALEXOV, A., BRETON, R. P., BILOUS, A. V., COOPER, S., FALCKE, H., GRIESSMEIER, J. M., HASSALL, T. E., HESSELS, J. W. T., KEANE, E. F., OSŁOWSKI, S., PILIA, M., SERYLAK, M., STAPPERS, B. W., TER VEEN, S., VAN LEEUWEN, J., ZAGKOURIS, K., ANDERSON, K., BÄHREN, L., BELL, M., BRODERICK, J., CARBONE, D., CENDES, Y., COENEN, T., CORBEL, S., EISLÖFFEL, J., FENDER, R., GARDEN, H., JONKER, P., LAW, C., MARKOFF, S., MASTERS, J., MILLER-JONES, J., MOLENAAR, G., OSTEN, R., PIETKA, M., ROL, E., ROWLINSON, A., SCHEERS, B., SPREEUW, H., STALEY, T., STEWART, A., SWINBANK, J., WIJERS, R., WIJNANDS, R., WISE, M., ZARKA, P. and VAN DER HORST, A. (2015). Pulsar polarisation below 200 MHz: Average profiles and propagation effects. *A&A* **576** A62. <https://doi.org/10.1051/0004-6361/201425186>

- PETROFF, E., HESSELS, J. W. T. and LORIMER, D. R. (2022). Fast radio bursts at the dawn of the 2020s. *A&A Rev.* **30** 2. <https://doi.org/10.1007/s00159-022-00139-w>
- PLATTS, E., WELTMAN, A., WALTERS, A., TENDULKAR, S. P., GORDIN, J. E. B. and KANDHAI, S. (2019). A living theory catalogue for fast radio bursts. *Phys. Rep.* **821** 1-27. <https://doi.org/10.1016/j.physrep.2019.06.003>
- PLEUNIS, Z., GOOD, D. C., KASPI, V. M., MCKINVEN, R., RANSOM, S. M., SCHOLZ, P., BANDURA, K., BHARDWAJ, M., BOYLE, P. J., BRAR, C., CASSANELLI, T., CHAWLA, P., (ADAM) DONG, F., FONSECA, E., GAENSLER, B. M., JOSEPHY, A., KACZMAREK, J. F., LEUNG, C., LIN, H.-H., MASUI, K. W., MENA-PARRA, J., MICHILLI, D., NG, C., PATEL, C., RAFIEI-RAVANDI, M., RAHMAN, M., SANGHAVI, P., SHIN, K., SMITH, K. M., STAIRS, I. H. and TENDULKAR, S. P. (2021). Fast Radio Burst Morphology in the First CHIME/FRB Catalog. *ApJ* **923** 1. <https://doi.org/10.3847/1538-4357/ac33ac>
- RAVI, V., CATHA, M., CHEN, G., CONNOR, L., CORDES, J. M., FABER, J. T., LAMB, J. W., HALLINAN, G., HARNACH, C., HELLBURG, G., HOBBS, R., HODGE, D., HODGES, M., LAW, C., RASMUSSEN, P., SHARMA, K., SHERMAN, M. B., SHI, J., SIMARD, D., SOMALWAR, J. J., SQUILLACE, R., WEINREB, S., WOODY, D. P. and YADLAPALLI, N. (2023). Deep Synoptic Array science: a 50 Mpc fast radio burst constrains the mass of the Milky Way circumgalactic medium. *arXiv e-prints* arXiv:2301.01000. <https://doi.org/10.48550/arXiv.2301.01000>
- SCHECHTER, P. (1976). An analytic expression for the luminosity function for galaxies. *ApJ* **203** 297-306. <https://doi.org/10.1086/154079>
- SHIN, K., MASUI, K. W., BHARDWAJ, M., CASSANELLI, T., CHAWLA, P., DOBBS, M., DONG, F. A., FONSECA, E., GAENSLER, B. M., HERRERA-MARTÍN, A., KACZMAREK, J., KASPI, V., LEUNG, C., MERRYFIELD, M., MICHILLI, D., MÜNCHMEYER, M., PEARLMAN, A. B., RAFIEI-RAVANDI, M., SMITH, K., STAIRS, I. and TENDULKAR, S. P. (2023). Inferring the Energy and Distance Distributions of Fast Radio Bursts Using the First CHIME/FRB Catalog. *ApJ* **944** 105. <https://doi.org/10.3847/1538-4357/acaf06>
- SPITLER, L. G., SCHOLZ, P., HESSELS, J. W. T., BOGDANOV, S., BRAZIER, A., CAMILO, F., CHATTERJEE, S., CORDES, J. M., CRAWFORD, F., DENEVA, J., FERDMAN, R. D., FREIRE, P. C. C., KASPI, V. M., LAZARUS, P., LYNCH, R., MADSEN, E. C., MCLAUGHLIN, M. A., PATEL, C., RANSOM, S. M., SEYMOUR, A., STAIRS, I. H., STAPPERS, B. W., VAN LEEUWEN, J. and ZHU, W. W. (2016). A repeating fast radio burst. *Nature* **531** 202-205. <https://doi.org/10.1038/nature17168>
- STENNING, D. C. and VAN DYK, D. A. (2018). Bayesian Statistical Methods for Astronomy. Part 2. Markov Chain Monte Carlo. In *Statistics for Astrophysics: Bayesian Methodology* (J.-B. Marquette, ed.) 29-58.
- VAN LIESHOUT, M. N. M. (2000). *Markov Point Processes and Their Applications. G - Reference, Information and Interdisciplinary Subjects Series*. Imperial College Press.
- ZHANG, B. (2022). The Physics of Fast Radio Bursts. *arXiv e-prints* arXiv:2212.03972. <https://doi.org/10.48550/arXiv.2212.03972>